

## A Conceptual Synoptic Model Approach to the Development of a Precipitation Climatology as Applied to Montreal, Quebec

KAI MELAMED-TURKISH,<sup>a</sup> SHAWN MILRAD,<sup>b</sup> JOHN GYAKUM,<sup>c</sup> AND EYAD ATALLAH<sup>d</sup>

<sup>a</sup> *Meteorological Service of Canada, Montreal, Quebec, Canada*

<sup>b</sup> *Applied Aviation Sciences Department, Embry-Riddle Aeronautical University, Daytona Beach, Florida*

<sup>c</sup> *Department of Atmospheric and Oceanic Sciences, McGill University, Montreal, Quebec, Canada*

<sup>d</sup> *Department of Hydrology and Atmospheric Sciences, The University of Arizona, Tucson, Arizona*

(Manuscript received 23 August 2021, in final form 19 April 2022)

**ABSTRACT:** This study documents the frequency and intensity of precipitation at Montreal, Canada, from 1979 to 2018 as it relates to four quadrants of a 500-hPa wave, identified by the position of troughs, ridges, and inflection points. These quadrants provide a simplified conceptualization of the contributions from the temperature and vorticity advection forcing terms in the quasigeostrophic (QG) omega equation. Precipitation is found to be significantly more intense in every season except summer in the quadrant immediately upstream of the 500-hPa ridge, where differential cyclonic vorticity advection (DCVA) and a local maximum in horizontal warm-air advection (WAA) tend to promote unambiguous QG ascent. In summer, the average precipitation is still most intense in the DCVA-WAA quadrant, but not significantly more than in the quadrant immediately downstream of the 500-hPa trough, where DCVA and a local maximum in horizontal cold-air advection (CAA) are expected to compete, resulting in ambiguous QG vertical motion. Precipitation in the DCVA-CAA quadrant is more intense in every season than in the expected differential anticyclonic vorticity advection (DAVA) quadrants, with significantly higher intensities in spring and fall. Furthermore, the DCVA quadrants exhibit significantly stronger ascent compared to the DAVA quadrants and the DCVA-WAA quadrant features significantly warmer 850-hPa equivalent potential temperatures compared to the three other quadrants in every season. Odds ratios indicate a statistically significant association between heavy precipitation episodes and the DCVA-WAA quadrant. Heavy precipitation episodes in the DCVA-CAA quadrant are associated with a negatively tilted 500-hPa geopotential height pattern in winter and fall.

**SIGNIFICANCE STATEMENT:** Operational weather forecasters apply conceptual models that connect upper-atmospheric weather patterns to vertical motion and precipitation. However, few studies have quantified this connection over a longer, continuous period of time. In this study, we examine the relationship between historical subdaily precipitation at Montreal, Canada, and a simple large-scale conceptual model that relates vertical motion to the position of upper-level troughs and ridges. We find significant evidence for heavy precipitation to occur upstream of the upper-level ridge, and for very little, or very light, precipitation to occur upstream of the upper-level trough. These results provide quantitative support to some of the conceptual methods available to operational weather forecasters in preliminary analyses that support their precipitation forecasts.

**KEYWORDS:** Forecasting techniques; North America; Precipitation; Quasigeostrophic models; Synoptic climatology; Synoptic-scale processes

### 1. Motivation and background

Precipitation can be socially and economically disruptive, from misjudging whether or not to bring an umbrella to work, to a catastrophic ice storm shutting down power to homes for weeks (Regan 1998; Soulard 1998). Predicting precipitation presents a significant challenge for forecasters. Meteorologists apply a wide array of forecasting techniques to improve quantitative precipitation forecasts (QPF), including: experience, knowledge of local effects and climatology, and simplified conceptual models. Simple conceptual models can be particularly useful in a meteorologist's preliminary, synoptic-scale analysis of the current and expected conditions.

A 500-hPa geopotential height chart is one of the principal charts that an operational weather forecaster analyzes. This chart is often used to identify planetary waves as well as shortwaves and areas of maximum and minimum cyclonic vorticity. This analysis can provide meteorologists with a rough sketch of the potential extent of midlevel clouds and precipitation based on the simplest conceptualization of the quasigeostrophic omega (hereafter, QG- $\omega$ ) equation for vertical motion.

Equation (1) shows the adiabatic frictionless form of the QG- $\omega$  equation [Eq. (5.6.11) from Bluestein 1992]; term A is the three-dimensional Laplacian of omega, term B represents the differential geostrophic advection of the geostrophic absolute vorticity (DVA), and term C is the horizontal Laplacian of geostrophic temperature advection (LTA):

*Corresponding author:* Shawn Milrad, milrads@erau.edu

DOI: 10.1175/WAF-D-21-0139.1

© 2022 American Meteorological Society. For information regarding reuse of this content and general copyright information, consult the [AMS Copyright Policy](#) ([www.ametsoc.org/PUBSReuseLicenses](http://www.ametsoc.org/PUBSReuseLicenses)).

$$\underbrace{\left(\nabla_p^2 + \frac{f_0^2}{\sigma} \frac{\partial^2}{\partial p^2}\right)}_A \omega = - \underbrace{\frac{f_0}{\sigma} \frac{\partial}{\partial p} [-\mathbf{v}_g \cdot \nabla_p (\zeta_g + f)]}_B - \underbrace{\frac{R}{\sigma P} \nabla_p^2 (-\mathbf{v}_g \cdot \nabla_p T)}_C, \quad (1)$$

where  $\sigma$  is the static stability parameter,  $\omega$  is the vertical velocity in pressure coordinates,  $f_0$  is the Coriolis parameter,  $f$  is planetary vorticity,  $\mathbf{v}_g$  is the geostrophic wind vector,  $\zeta_g$  is the geostrophic relative vorticity,  $T$  is temperature,  $R$  is the gas constant for dry air, and the Laplacians and gradients are applied on a constant pressure surface. For continuous fields subject to Fourier decomposition, omega can be diagnosed from a linear combination of the negative of terms B and C. This is generally the case for synoptic-scale systems in the midtroposphere (Trenberth 1978; Durran and Snellman 1987), and implies that synoptic-scale vertical motions are a result of DVA and LTA.

Operational meteorologists often simplify term B to vorticity advection (VA) at one level and term C to  $-1$  times the temperature advection (TA) in order to qualitatively diagnose vertical motion (Billingsley 1997). However, through a case study, Durran and Snellman (1987) illustrated that the VA at one level is not necessarily the same as DVA. Moreover, they demonstrated that  $-1$  times the TA is not necessarily the same as the LTA. Nonetheless, Dookhie (2011) noted that while terms B and C in Eq. (1) were not as quantitatively useful as the vertical motion obtained from the Q-vector form of the QG- $\omega$  equation (Hoskins et al. 1978), they still offered qualitative insight into the large-scale features contributing to vertical motion. Conversely, in their case study on anomalous snowfall during an Alberta Clipper, Rochette et al. (2017) found that the vertical motion implied by the Q-vector form of the QG omega equation (which combines the DVA and LTA terms into an unambiguous single forcing term) was inconclusive while the VA at 500 hPa and the TA at 850 hPa were useful diagnostics for vertical motion. Since this paper uses a forecaster's framework, we apply the assumption that vertical motion can be qualitatively diagnosed based on the VA at one level and the negative of TA.

Following the analyses of Bluestein (1992) and Funk (2011) on Eq. (1), we can divide a 500-hPa wave into four conceptual quadrants based on the locations of the trough and ridge axes, and the respective inflection points (conceptual positions of low-level cyclones and anticyclones). The result is the simple conceptual schematic shown in Fig. 1. As in Bluestein (1992) and Funk (2011), Eq. (1) then enables us to qualitatively diagnose generalized regions of: differential cyclonic vorticity advection (DCVA) and a horizontal maximum in cold air advection (CAA; quadrant CyC), DCVA and a horizontal maximum in warm air advection (WAA; quadrant CyW), differential anticyclonic vorticity advection (DAVA) and WAA (quadrant AnW), and DAVA and CAA (quadrant AnC).

Operational meteorologists can apply Fig. 1 of Trenberth (1978) in their preliminary analyses to note that synoptic-scale precipitation generally occurs between the upstream 500-hPa

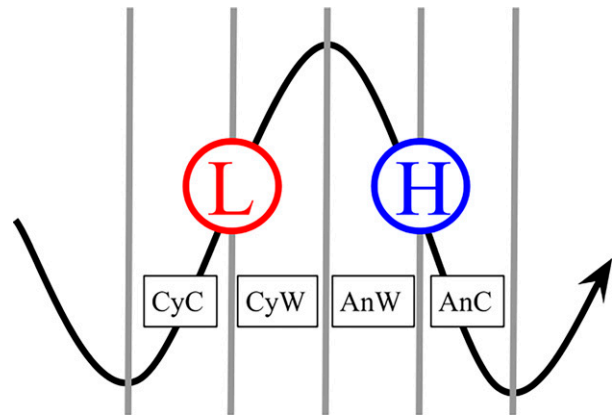


FIG. 1. Schematic of a 500-hPa westerly wave. The “L” represents the approximate location of a low-level cyclone and the “H” represents the approximate location of a low-level anticyclone. Assuming that the 1000–500-hPa thickness contours are in phase with the 500-hPa geopotential heights, we can infer the following from the QG- $\omega$  equation [Eq. (1)]. Quadrant AnC: differential anticyclonic vorticity advection (DAVA) and a horizontal maximum in cold-air advection (CAA)  $\rightarrow$  Unambiguous QG forcing for descent. Quadrant AnW: DAVA and a horizontal maximum in warm-air advection (WAA)  $\rightarrow$  ambiguous QG vertical motion. Quadrant CyW: differential cyclonic vorticity advection (DCVA) and WAA  $\rightarrow$  unambiguous QG forcing for ascent. Quadrant CyC: DCVA and CAA  $\rightarrow$  ambiguous QG vertical motion.

trough and downstream 500-hPa ridge. Meteorologists may then refer to the schematic in our Fig. 1 to highlight the potential for moderate to strong synoptic-scale forcing for precipitation between the 500-hPa ridge and the inflection point immediately upstream. The inflection point as a point of interest for more intense precipitation also corresponds well to the maximum in upward motion noted in Fig. 1 of Trenberth (1978).

Consequently, the conceptual model presented in our Fig. 1 can be an extremely useful tool in a meteorologist's preliminary analysis. A quick analysis of the 500-hPa geopotential heights can allow a meteorologist to assess whether their forecast region resides in a favorable region for synoptic-scale ascent forcing and precipitation. Moreover, meteorologists can also make short- to medium-range predictions of their cloud and precipitation zones based on the 500-hPa geopotential height pattern. For short-range forecasts, this can be done using forecasting techniques such as extrapolation, while numerical weather prediction (NWP) model forecast 500-hPa geopotential heights can be used for medium-range forecasts, since 500-hPa heights are generally well-predicted (Roebber and Bosart 1998; Sisson and Gyakum 2004).

The primary objective of this study is to investigate whether the simple conceptual model in Fig. 1 conveys meaningful information about precipitation behavior for a midlatitude North American city. Through a 40-yr climatology, we aim to assess whether precipitation in Montreal, Quebec, Canada, occurs primarily in the CyC, CyW, and AnW quadrants and whether or not a maximum (minimum) in precipitation intensity occurs in the CyW (AnC) quadrant. There are limitations

to our approach, such as not evaluating subsynoptic ascent-forcing mechanisms, and particularly at midlatitude locations where convection is a dominant factor in heavy precipitation during at least one season. However, our results can provide operational weather forecasters with a simple framework to better anticipate precipitation episodes or at least provide climatological support for methods already used as part of the analysis process. This may be particularly beneficial at midlatitude locations where synoptic-scale ascent-forcing mechanisms are crucial to heavy precipitation events. The climatological evaluation of this simplified QG conceptualization could also provide supporting material in educational settings, as this conceptual model represents a cornerstone in university-level synoptic–dynamic meteorology (e.g., [Bluestein 1992](#), p. 331).

The novel approach presented here differs from previous precipitation climatologies. Many earlier studies applied a variety of temporal criteria and constraints to identify precipitation events (e.g., [Konrad 1997](#); [Fischer 1998](#); [Akinremi et al. 1999](#); [Kunkel et al. 1999](#); [Sisson and Gyakum 2004](#); [Wang and Zhou 2005](#); [Yu et al. 2007](#); [Milrad et al. 2009, 2014](#)) in order to analyze their synoptic and climatological characteristics. As examples, [Sisson and Gyakum \(2004\)](#) identified 24-h precipitation events at Burlington, Vermont, and analyzed the synoptic–dynamic characteristics of various event categories (e.g., heavy), while [Milrad et al. \(2014\)](#) performed a similar analysis for warm-season precipitation events lasting between 6 and 72 h at Montreal. Other precipitation climatologies have applied statistical methods to identify precipitation events (e.g., [Fukutome et al. 2015](#); [Moore et al. 2015, 2019](#); [Barton et al. 2016](#)). For example, [Moore et al. \(2015, 2019\)](#) used precipitation percentiles (e.g., 99th, 99.5th) at a grid point to define extreme precipitation events in the central and eastern United States. While the aforementioned studies provide valuable information about precipitation events identified through spatiotemporal or statistical methods, we use a forecaster’s framework in the initial identification of precipitation episodes. Consequently, our precipitation episodes inherently contain meteorologically relevant information whereas prior methods required further analysis of the identified precipitation events. For a more extensive review on the various methodologies used to identify precipitation events, particularly extreme events, see the [Barlow et al. \(2019\)](#) review paper. The remainder of the paper is organized as follows: [section 2](#) outlines the data and methodology used to create the precipitation climatology, [sections 3–6](#) present the climatology results, and [section 7](#) provides some conclusions and future work.

## 2. Data and methods

### a. Data

For Montreal’s Pierre Elliott Trudeau International Airport (CYUL), we used 6-h precipitation data from 1979 to 2018. Data for 1979–2008 were provided by the authors of [Milrad et al. \(2014\)](#); 2009–18 data were obtained using archived surface synoptic (SYNOP) observations. SYNOP is an older

(compared to METAR) numerical code-based surface observation reporting system called FM-12 by the WMO, and still used at thousands of stations worldwide. Included in the SYNOP reports is 6-h precipitation accumulation. The precipitation data used from the archived synoptic reports before 2009 were corroborated with the [Milrad et al. \(2014\)](#) data to ensure consistency and accuracy. We used 500-hPa geopotential heights from the North American Regional Reanalysis (NARR; [Mesinger et al. 2006](#)) at the grid point closest to CYUL (CYUL is located at 45.47°N, 73.75°W, and the closest NARR grid point is at 45.45°N, 73.77°W) to identify the quadrants depicted in [Fig. 1](#). The NARR has a 32-km horizontal grid spacing, 29 pressure levels between 1000 and 100 hPa, a temporal resolution of 3 h, and is available from 1979 to the present.

### b. Identifying quadrants and partitioning precipitation data

To identify the four quadrants of the 500-hPa wave pattern, local maxima/minima and inflection points were identified based on the first and second time derivatives, respectively, of the 500-hPa geopotential heights at CYUL. Given the inherent noise in the derivatives of the 500-hPa geopotential height field, we developed a data smoothing process. First, we calculated 6-h means of the original 3-h 500-hPa geopotential heights in order to be consistent with the 6-h precipitation accumulated over the same period. For example, if the precipitation episode window was 0000–0600 UTC, we used the 6-h mean of geopotential height for the 0000–0600 UTC period. We then smoothed the 6-h data using a Gaussian-weighted moving average with a window length of 24 h (or four data points) on either side of the element being smoothed. In other words, a total of nine elements were included in the Gaussian-weighted moving average centered about element five. We tested other smoothing methods and window lengths, but the Gaussian-weighted moving average with a window length of nine was the most successful at smoothing out the noise while preserving the desired longer wavelengths. Specifically, the wavelengths identified by this method generally reside within the synoptic scale (~1–10 days).

Once the four quadrants were identified, the measurable 6-h precipitation accumulations ( $\geq 0.2$  mm) were grouped into their corresponding quadrants. [Figure 2](#) illustrates how this method works during a 17-day period during 10–26 January 1999. This sample period was chosen because measurable precipitation occurred in each of the four quadrants within one 500-hPa wavelength. [Figure 2a](#) shows how the 6-h precipitation accumulations (blue bars) are sorted into their corresponding quadrants based on the smoothed, 6-h mean 500-hPa geopotential height standardized anomalies (black curve). [Figures 2b–e](#) illustrate the correspondence between the time series and the spatial maps on the evolution of the 500-hPa wave pattern over CYUL. Comparison between other samples from the time series and spatial maps (not shown) confirm that the time series of the smoothed, 6-h mean 500-hPa geopotential heights adequately represents the evolution of synoptic-scale waves over CYUL.

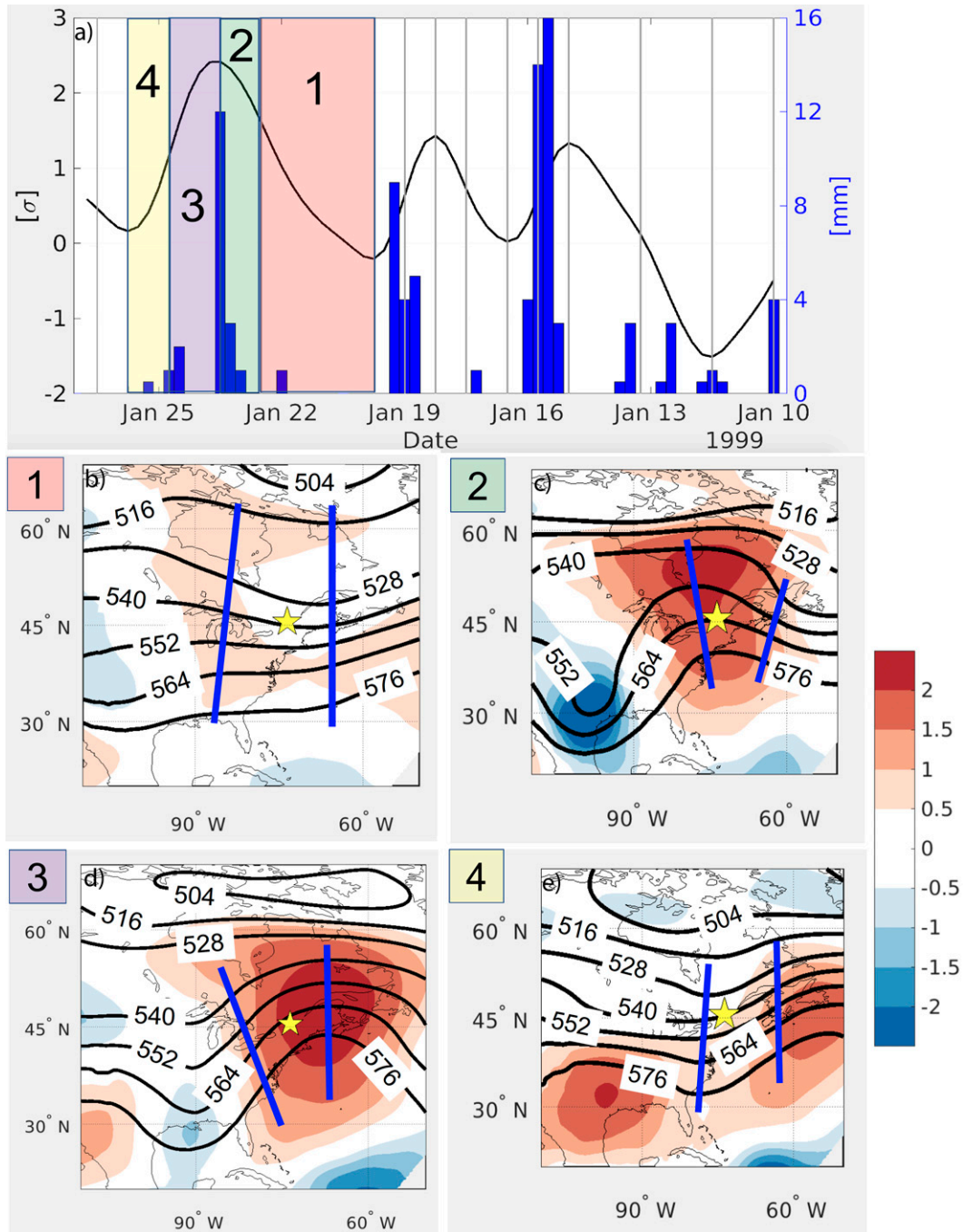


FIG. 2. (a) 500-hPa geopotential height standardized anomalies (black curve; left y axis) and 6-h precipitation amounts (mm; blue bars; right y axis) for CYUL from 10 to 26 Jan 1999. Vertical gray lines denote the time of trough, ridge, and inflection point passages. Quadrant AnC is shaded in red and marked with a 1, quadrant AnW is shaded in green and marked with a 2, quadrant CyW is shaded in purple and marked with a 3, and quadrant CyC is shaded in yellow and marked with a 4. (b) 500-hPa geopotential height composite mean (dam; solid black contours) and composite standardized anomalies (shaded) for quadrant AnC highlighted and labeled in (a). (c) As in (b), but for quadrant AnW. (d) As in (b), but for quadrant CyW. (e) As in (b), but for quadrant CyC. The yellow stars and solid blue lines in (b)–(e) demark the location of CYUL and quadrant boundaries, respectively.

TABLE 1. Precipitation amounts (mm) and percentile ranges for heavy, moderate, light, and very light quadrant precipitation episodes.

Intensity category	Percentile range	Precipitation amount range (mm)			
		DJF	MAM	JJA	SON
Heavy	90th–100th	14–58.0	16.4–58	21.6–87.2	18–134.5
Moderate	70th–80th	5–7.6	7–10	8.2–12.6	7.8–12
Light	45th–55th	1.8–2.6	2.6–4	3–5	3–4.4
Very light	0th–25th	0.6	1	1	1

c. Statistical analysis

To compare the physical characteristics of the quadrants, we apply an analysis of variance (ANOVA) and then Scheffé’s procedure (Kutner et al. 2005) to seasonal quadrant precipitation, 500-hPa  $\omega$ , and 850-hPa  $\theta_e$  standardized anomalies. We also apply this method for convective stability ( $\sigma_e$ ) between 500 and 850 hPa, calculated as

$$\sigma_e = \theta_{e500} - \theta_{e850}, \tag{2}$$

where  $\sigma_e$  is the convective stability, and  $\theta_{e500}$  and  $\theta_{e850}$  are the equivalent potential temperatures at 500 and 850 hPa, respectively. For precipitation, the ANOVA and Scheffé’s procedure are applied to both quadrant period totals and maximum 6-h rates. For the other three atmospheric variables ( $\omega$ ,  $\theta_e$ , and  $\sigma_e$ ), we apply the ANOVA and Scheffé’s procedure to quadrant-mean values as well as the value at the time step just prior to the quadrant period maximum 6-h precipitation rate. This means that if the quadrant period maximum 6-h precipitation rate occurs between 0000 and 0600 UTC, the 0000 UTC values of  $\omega$ ,  $\theta_e$ , and  $\sigma_e$  are the ones included in the computation.

For each individual atmospheric variable (e.g.,  $\omega$ ; sections 4a–d), comparison intervals from Scheffé’s procedure illustrate which means are significantly different from one another at the  $\alpha = 0.05$  significance level. For the purposes of this study, we illustrate the interquadrant multiple comparisons within a given season. For example, if the comparison interval of the winter quadrant CyC mean lies outside the winter comparison intervals for quadrants AnC, AnW, and CyW, then we can conclude that the CyC mean is statistically different than the means of the three other quadrants at the  $\alpha = 0.05$  significance level. For comparison intervals that appear close to each other, we verified whether or not the p value was less than 0.05. We use the climatological seasons, such that winter encompasses December–February (DJF), spring March–May (MAM), summer June–August (JJA), and fall September–November (SON). Hereafter, the application of Scheffé’s procedure to the seasonal quadrant data are referred to as the Scheffé seasonal quadrant comparison.

We define precipitation intensity categories as in Milrad et al. (2014) using quadrant-period precipitation totals. Heavy precipitation episodes compose the top 10% of precipitation episodes (90th–100th percentile range) within a meteorological season, moderate episodes span the 70th–80th percentile range, light episodes span the 45th–55th percentile range, and very light episodes the 0th–25th percentile range (Table 1).

Very light episodes are presented for climatological information (Table 1), but are not discussed throughout the majority of our analysis.

We use odds ratios (ORs; Wilks 2006) to determine the statistical association between precipitation episodes of three intensity categories (light, moderate, and heavy) and the four quadrants. ORs are calculated as in Eq. (7.9) in Wilks (2006):

$$OR = \frac{P(Q)[1 - P(N)]}{P(N)[1 - P(Q)]}, \tag{3}$$

where  $P(Q)$  is the conditional probability of occurrence of a precipitation episode of specified intensity given that Montreal is in a specific quadrant (e.g., quadrant CyW),  $P(N)$  is the conditional probability of occurrence of a precipitation episode of specified intensity given that Montreal is not in the previously specified quadrant and is calculated for all episodes in the three other quadrants (in the example above, quadrants AnC, AnW, and CyC). To compute these probabilities, all quadrant periods, both with and without measurable precipitation, must be included. An  $OR > 1$  indicates a positive association between precipitation episodes of specified intensity and the specified quadrant. Specifically, the likelihood of a precipitation episode of that intensity is enhanced when Montreal is in the specified quadrant relative to when Montreal is not in that quadrant. An  $OR < 1$  indicates a negative association, such that the likelihood of a precipitation episode of specified intensity is reduced when Montreal is in the specified quadrant relative to when Montreal is not in that quadrant. An OR of 1 indicates that precipitation episodes of the specified intensity and the specified quadrant are independent events.

The standard deviation of the OR as presented in Eq. (7.68) in Wilks (2006) can be used to compute the upper and lower confidence intervals:

$$CI_{OR_{upper}} = \exp \left[ \ln(OR) + z_{\alpha/2} \left( \sqrt{\frac{1}{N_1} + \frac{1}{N_2} + \frac{1}{N_3} + \frac{1}{N_4}} \right) \right], \tag{4}$$

$$CI_{OR_{lower}} = \exp \left[ \ln(OR) - z_{\alpha/2} \left( \sqrt{\frac{1}{N_1} + \frac{1}{N_2} + \frac{1}{N_3} + \frac{1}{N_4}} \right) \right], \tag{5}$$

where  $CI_{OR_{upper}}$  and  $CI_{OR_{lower}}$  are the upper and lower confidence intervals on the OR,  $\alpha$  represents the level of significance,  $z_{\alpha/2}$  represents the z score at  $\alpha/2$ ,  $N_1$  represents the

TABLE 2. Number of quadrant periods with measurable precipitation by meteorological season (DJF, MAM, JJA, and SON). The percentage of all quadrant periods with measurable precipitation is shown in parentheses in the last row.

No. of quadrant precipitation episodes	AnC	AnW	CyW	CyC
DJF	321	241	627	635
MAM	281	219	521	522
JJA	276	156	453	519
SON	242	163	494	560
Total	1120 (33%)	779 (23%)	2095 (62%)	2236 (66%)

number of precipitation events in the specified intensity category that occurred in the specified quadrant,  $N_2$  represents the number of precipitation events in the specified intensity category that occurred in the three other quadrants,  $N_3$

represents the number of quadrant periods not in the specified intensity category that occurred in the specified quadrant, and  $N_4$  represents the number of quadrant periods not in the specified intensity category that occurred outside of the

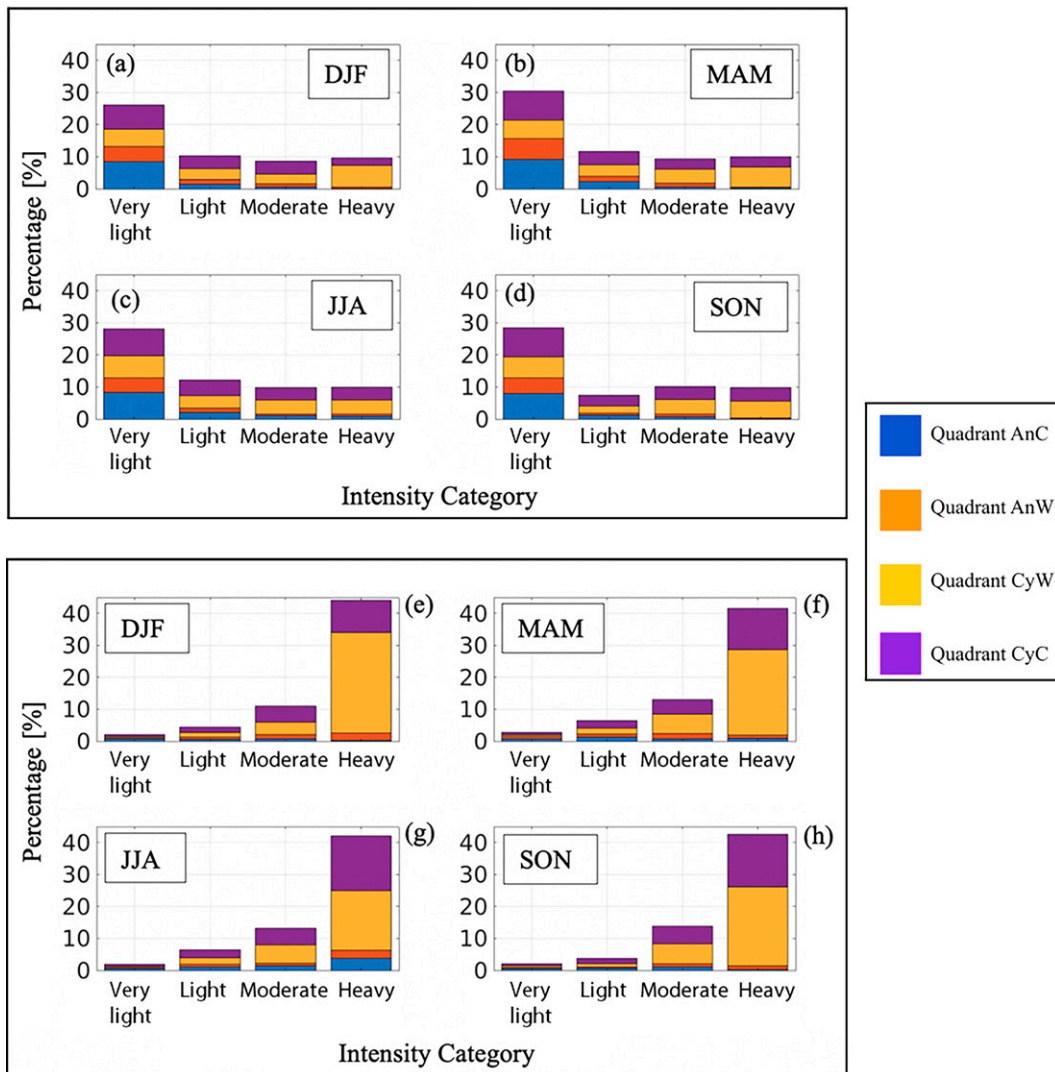


FIG. 3. The percentage of measurable precipitation events (y axis) by categorical [very light (0th–25th percentile), light (45th–55th percentile), moderate (70th–80th percentile), and heavy (90th–100th percentile)] quadrant precipitation episodes (x axis) and quadrant (legend, right) to (a) DJF, (b) MAM, (c) JJA, and (d) SON. (e)–(h) As in (a)–(d), but for the percentage contribution by intensity category and quadrant to the cumulative total seasonal precipitation.

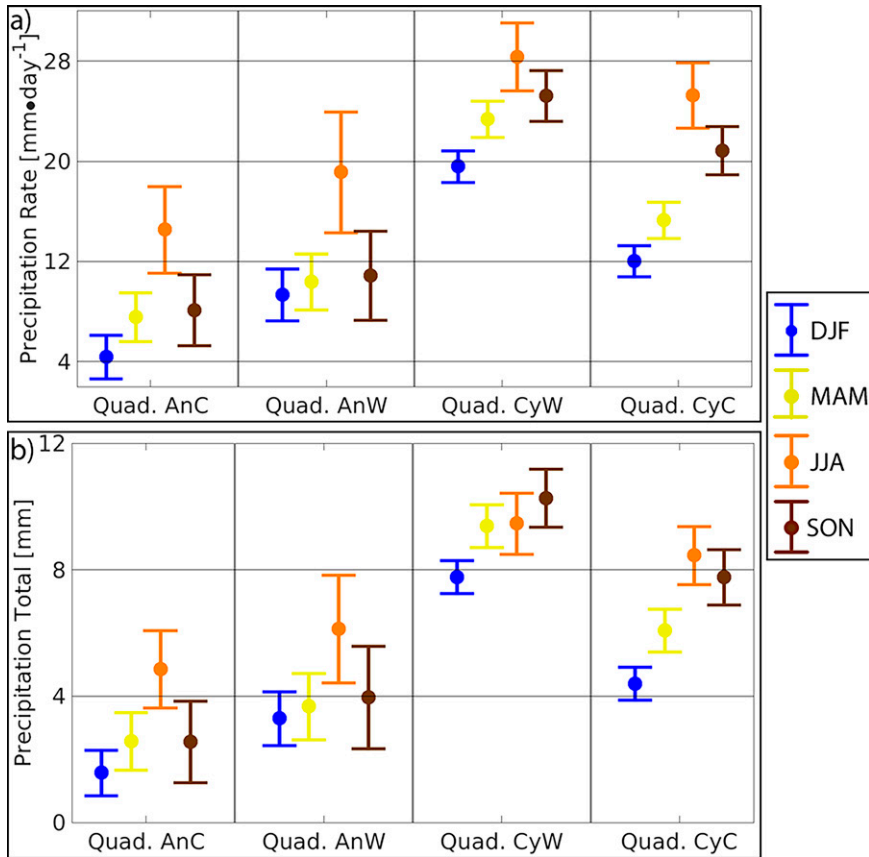


FIG. 4. (a) The average maximum precipitation rate ( $\text{mm day}^{-1}$ ) for all measurable precipitation episodes in each quadrant and each season. The central bullet in each of the bars represents the 40-yr arithmetic mean for each quadrant and each season. The bars extending from the central bullet represent  $\alpha = 0.05$  level of significance interquadrant comparison intervals. (b) As in (a), but for the average precipitation totals (mm). The legend illustrates the color coding for each season: blue for winter, yellow for spring, orange for summer, and brown for fall.

quadrant in question. We use the  $\alpha = 0.05$  level of significance (95% confidence intervals) to determine whether the OR is significantly higher or lower than 1.

d. Synoptic composites

Using the NARR, we produced composites of synoptic-scale parameters (e.g., 500-hPa geopotential height standardized anomalies, mean sea level pressure (MSLP), 850-hPa  $\theta_e$  standardized anomalies; section 6) for the light, moderate, and heavy winter precipitation episodes at the onset time of the maximum 6-h precipitation period during an episode. Standardized anomalies were calculated relative to a 1979–2018 NARR climatology for the date of maximum precipitation during an individual precipitation episode. Individual standardized anomalies were calculated by subtracting the daily NARR values of a variable (e.g., geopotential height) from the daily NARR climatology (1979–2018) of that variable for the date of interest and then dividing by the daily climatology’s standard deviation (for more on using standardized anomalies in synoptic composites, see e.g., Grumm and

Hart 2001). We obtained the composite mean standardized anomalies in a precipitation episode category by compositing the individual standardized anomalies from each event in that category. For the sake of brevity, only quadrant CyC composites are shown (section 6).

3. Climatological summary

For 1979–2018, we identified 6230 quadrant periods with at least one 6-h precipitation accumulation of  $\geq 0.2$  mm, hereafter referred to as a quadrant precipitation episode. With this definition, ~46% of all quadrant periods were quadrant precipitation episodes. Approximately 18% of quadrant precipitation episodes occurred in quadrant AnC, 12% in quadrant AnW, 34% in quadrant CyW, and 36% in quadrant CyC (Table 2). More than 60% of all quadrant CyW and CyC periods were precipitation episodes, while only approximately one-third of all the quadrant AnC periods, and less than a quarter of all quadrant AnW periods were precipitation episodes.

Figures 3a–d display the relative frequency (expressed as a percentage) of quadrant precipitation episodes in the very

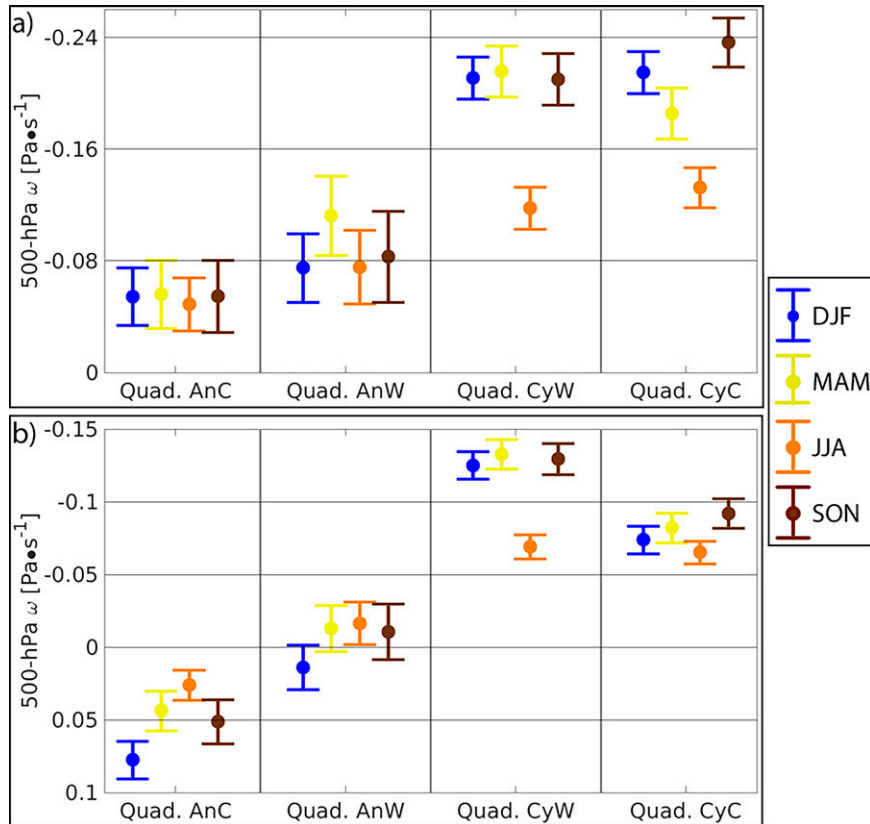


FIG. 5. (a) As in Fig. 4a, but for the average 500-hPa  $\omega$  ( $\text{Pa s}^{-1}$ ) at the 6-h time step prior to the maximum 6-h precipitation for all measurable precipitation episodes in each quadrant. (b) As in (a), but for the quadrant period mean 500-hPa  $\omega$  ( $\text{Pa s}^{-1}$ ).

light, light, moderate, and heavy precipitation categories (Table 1). The percentages in each panel of Fig. 3 do not add up to 100% because some percentiles are not included in any category (Table 1). Figures 3a–d illustrate a fairly even partitioning among quadrants CyW and CyC in the frequency of light and moderate precipitation episodes, while the majority of heavy precipitation episodes occurred in quadrant CyW. Quadrant CyC had the second-highest frequency of heavy precipitation episodes in every season with comparable frequencies to quadrant CyW in the summer (Fig. 3c). Conversely, a larger portion of quadrant CyC precipitation episodes lie in the very light category compared to quadrant CyW precipitation episodes. These results imply that even though quadrant CyC had the most precipitation episodes, the conditions for heavy precipitation to occur are most favorable in quadrant CyW. This last finding coincides with our expectations that unambiguous synoptic-scale ascent occurs in quadrant CyW (Fig. 1), as implied by the QG– $\omega$  equation [Eq. (1)]. During the summer, however, the overall conditions for heavy precipitation to occur are equally favorable in both quadrants CyW and CyC.

The majority of quadrant AnC precipitation episodes occur in the very light category (Figs. 3a–d) with only one heavy precipitation episode in the winter, four in the spring,

and none in the fall. Therefore, while precipitation can occur in quadrant AnC, conditions for moderate and heavy precipitation appear to be unfavorable, especially in winter, spring, and fall. This also coincides with our expectations for unambiguous synoptic-scale descent in quadrant AnC (Fig. 1). Quadrant AnW has the lowest frequency of measurable precipitation episodes, regardless of intensity (Figs. 3a–d). This implies that conditions are generally not favorable for precipitation in quadrant AnW. However, quadrant AnW has more heavy precipitation episodes than quadrant AnC in all seasons except summer, likely because unlike in quadrant AnC (unambiguous synoptic-scale descent), ambiguous vertical motion is expected in quadrant AnW, meaning that some synoptic-scale ascent can occur at times. This implies more favorable conditions for heavy precipitation to occur in quadrant AnW compared to quadrant AnC during the seasons when synoptic-scale mechanisms for ascent play a larger role in the development of heavy precipitation. Nonetheless, we might have expected less disparity between quadrants AnW and CyC, both in the total number of precipitation episodes (Table 2) and within the different intensity categories (Figs. 3a–d), because both quadrants have competing QG mechanisms for vertical motion (Fig. 1). Sections 4b–d elaborate further on

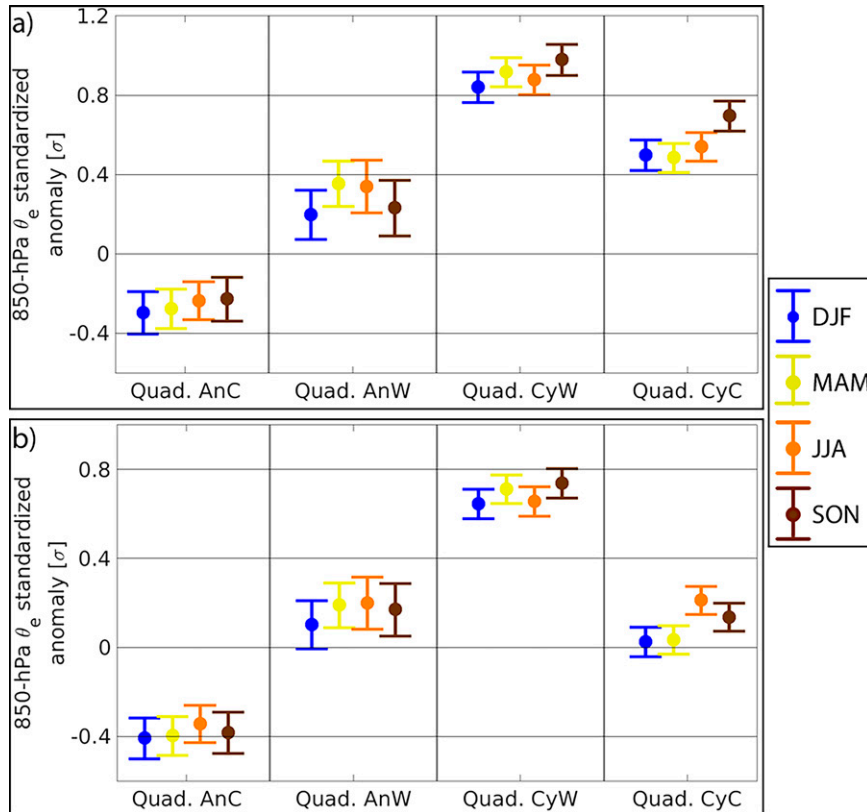


FIG. 6. As in Fig. 5, but for 850-hPa  $\theta_e$  standardized anomalies ( $\sigma$ ).

the atmospheric conditions and the QG mechanisms for vertical motion present in each quadrant.

To better understand the hydrological importance of the intensity categories, we also investigated each of their contributions to the cumulative seasonal precipitation total (Figs. 3e–h). Despite heavy precipitation episodes only composing approximately 10% of all measurable precipitation episodes, they contribute the most (>40%) to each season’s cumulative precipitation total. Moreover, the light and very light categories combined only contribute approximately 10% or less to each season’s cumulative precipitation total. Given the higher frequency of heavy precipitation episodes in quadrant CyW, it follows that quadrant CyW episodes contribute the most to each season’s cumulative precipitation total, except in summer when quadrants CyW and CyC contribute approximately equal amounts. These results affirm the hydrological importance of heavy precipitation episodes and indicate that quadrant CyW, and to a certain extent, quadrant CyC precipitation episodes, require particular consideration regarding their potential hydrological impacts.

#### 4. Analysis of variance (ANOVA)

##### a. Precipitation

Figure 4a shows the Scheffé seasonal quadrant comparison of the average maximum precipitation rate ( $P_m$ ) for

all quadrant precipitation episodes. The rate  $P_m$  is computed as

$$P_m = \overline{(P_{r_{max}})_{\text{quadrant}}}, \tag{6}$$

where  $P_m$  represents the seasonal average maximum quadrant period precipitation rate for 1979–2018, and  $(P_{r_{max}})_{\text{quadrant}}$  is the maximum precipitation rate for a single quadrant period. The central bullet in each bar represents the arithmetic mean, while the bars extending from each bullet represent the inter-quadrant comparison intervals. Figure 4a demonstrates that  $P_m$  in quadrant CyW is significantly higher than the three other quadrants in winter, spring, and fall and the overall highest in all seasons. The  $P_m$  is significantly lower in quadrant AnC than in the three other quadrants in winter and is the overall lowest in all seasons. The results for  $P_m$  in quadrants AnC and CyW concur with those from Figs. 3e–h and our expectations from Fig. 1. The  $P_m$  is higher in quadrant CyW, and to a certain extent, quadrant CyC compared to quadrant AnW in all seasons, and significantly so in the spring and fall.

Figure 4b illustrates the Scheffé seasonal quadrant comparison as in Fig. 4a, but for the average quadrant precipitation episode precipitation totals ( $P_T$ ). The  $P_T$  is computed as

$$P_T = \overline{(P_T)_{\text{quadrant}}}, \tag{7}$$

where  $P_T$  represents the average quadrant precipitation episode precipitation total for 1979–2018, and  $(P_T)_{\text{quadrant}}$  is the

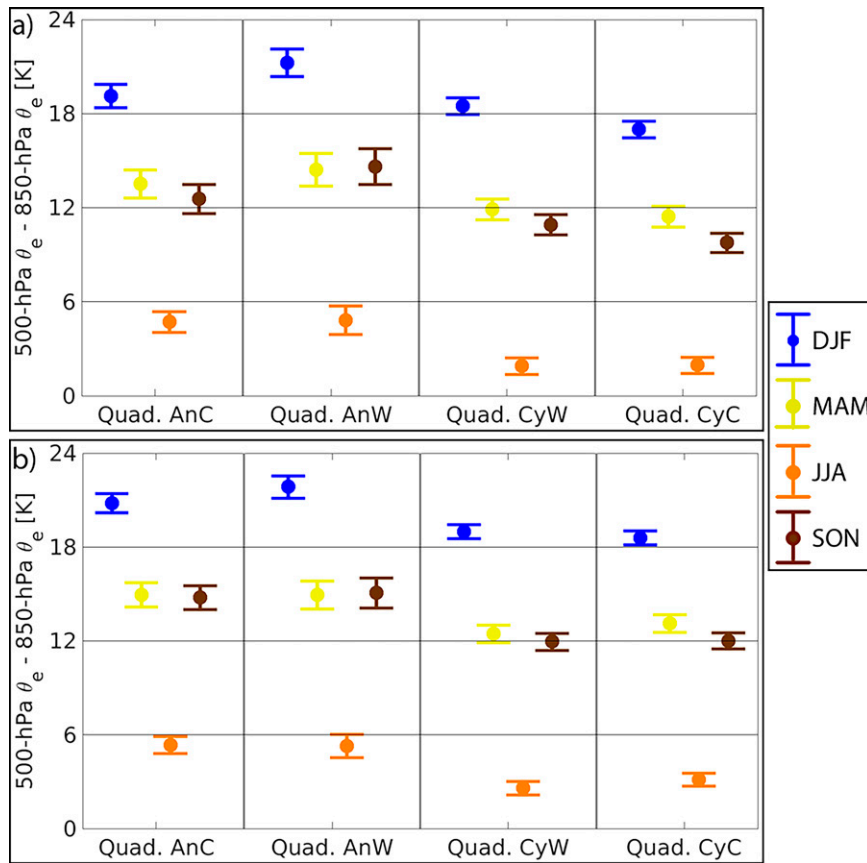


FIG. 7. As in Fig. 5, but for 850–500-hPa convective stability ( $\sigma_e$ ; K).

precipitation total for a single quadrant precipitation episode. The statistically significant interquadrant comparisons are the same as for  $P_m$ .

b. 500-hPa  $\omega$

Figure 5a shows the Scheffé seasonal quadrant comparison for 500-hPa  $\omega$  at the time step just prior to the maximum 6-h precipitation rate ( $\omega_m$ ). The  $\omega_m$  is computed as

$$\omega_m = \overline{(\omega_{p_m})_{\text{quadrant}}}, \tag{8}$$

where  $\omega_m$  represents the average quadrant period 500-hPa  $\omega$  at the time step just prior to the maximum 6-h precipitation rate for 1979–2018, and  $(\omega_{p_m})_{\text{quadrant}}$  is the 500-hPa  $\omega$  at the time step just prior to the maximum 6-h precipitation rate for a single quadrant period. Figure 5b illustrates the Scheffé seasonal quadrant comparison for the quadrant-mean values of 500-hPa  $\omega$  ( $\omega_T$ ) for quadrant precipitation episodes. The  $\omega_T$  is computed as

$$\omega_T = \overline{(\omega_T)_{\text{quadrant}}}, \tag{9}$$

where  $\omega_T$  represents the average quadrant period 500-hPa  $\omega$  for 1979–2018, and  $(\omega_T)_{\text{quadrant}}$  is the average 500-hPa  $\omega$  (including both ascent and descent) for a single quadrant precipitation episode. We find similar results in Figs. 5a and 5b in that quadrants CyW and CyC have significantly larger values of ascent than quadrants AnC and AnW in all seasons. However,

unlike with  $\omega_m$  (Fig. 5a), values of  $\omega_T$  (Fig. 5b) in quadrant CyW (AnW) are significantly more negative than in quadrant CyC (AnC) in all seasons (except summer for the CyW and CyC comparison). In general, the stronger ascent observed in quadrants CyW and CyC compared to quadrants AnC and AnW corresponds well to the precipitation results from Figs. 3 and 4. We also compared the values of ascent at 700 hPa and the level of maximum ascent and found similar results (not shown).

There is also relatively weak ascent in quadrants CyW and CyC in summer compared to the other seasons; significance for these results is drawn from the interseasonal comparisons and is not shown here. Specifically,  $\omega_m$  is significantly more positive in summer compared to the other seasons in quadrant CyC. In addition,  $\omega_T$  is significantly more positive in summer relative to the other seasons in quadrants CyC and CyW. These results likely highlight a convective signal and imply that a substantial portion of the ascent in summer occurs within convective systems as opposed to the synoptic-scale ascent that would be more dominant in the other seasons. The increased convection during summer may also help to explain why  $P_m$  and  $P_T$  are significantly higher in quadrant CyW compared to quadrant CyC in all seasons except summer.

c. 850-hPa  $\theta_e$  standardized anomalies

Figures 6a and b display the Scheffé seasonal quadrant comparison for the average 850-hPa  $\theta_e$  standardized anomalies at

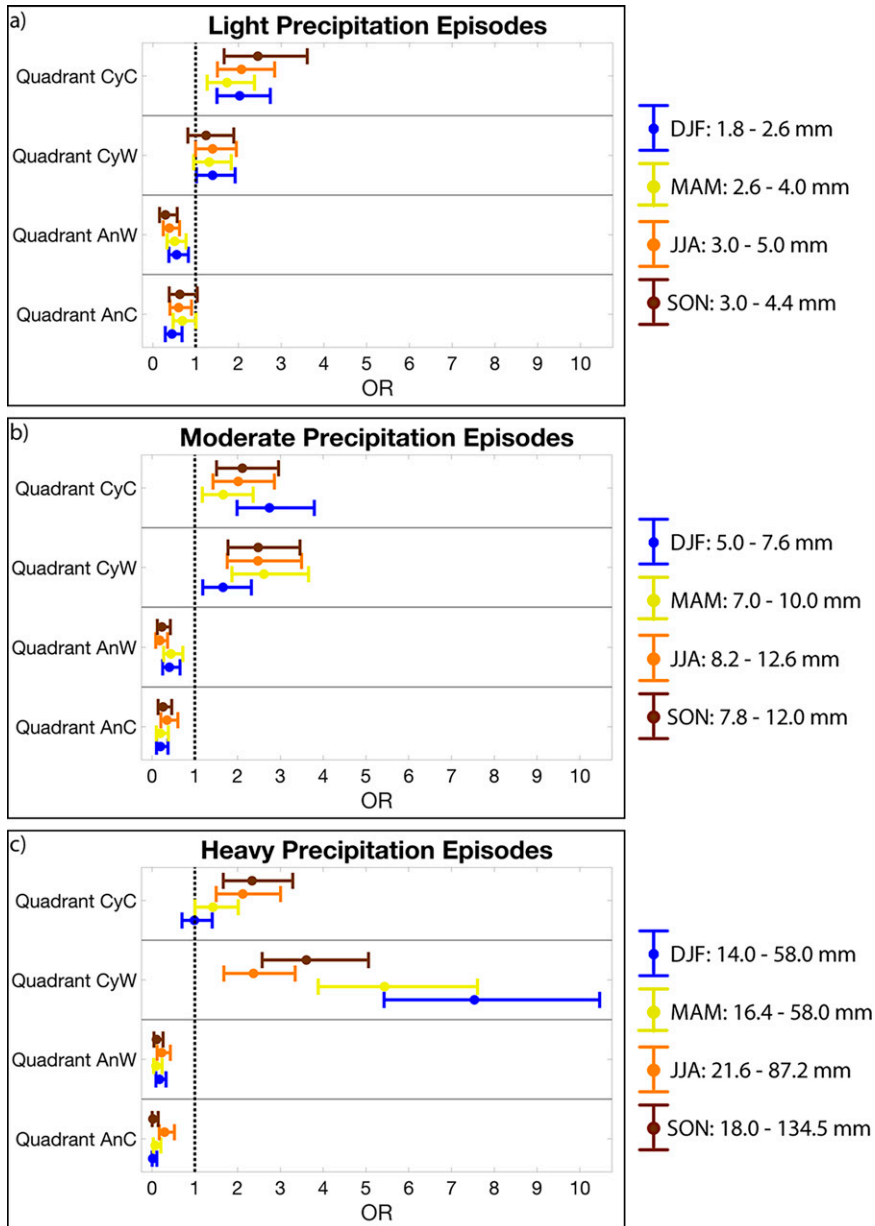


FIG. 8. ORs (bullets) and 95% CIs for (a) light (45th–55th percentile), (b) moderate (70th–80th percentile), and (c) heavy (90th–100th percentile) quadrant precipitation episodes. The quadrant precipitation episode totals (mm) associated with the different intensity categories for each season are shown in the legends.

the time step just prior to the maximum 6-h precipitation rate ( $\theta_{e_m}$ ) and the quadrant precipitation episode mean ( $\theta_{e_T}$ ), respectively. The  $\theta_{e_m}$  and  $\theta_{e_T}$  are computed as in Eqs. (8) and (9), but with 850-hPa  $\theta_e$  standardized anomalies. The  $\theta_{e_m}$  in quadrant CyW is significantly higher than in the other quadrants in all seasons, while  $\theta_{e_m}$  in quadrant AnC is significantly lower than in the other quadrants in all seasons. Quadrant CyC has a higher  $\theta_{e_m}$  than in quadrant AnW in all seasons, with significantly higher values in winter and fall. Results are similar for  $\theta_{e_T}$  (Fig. 6b) except that quadrant AnW has a

higher  $\theta_{e_T}$  than quadrant CyC in all seasons except summer, although results are not statistically significant.

The significantly higher 850-hPa  $\theta_e$  anomalies in quadrant CyW highlight its favorable thermodynamic conditions for heavy precipitation. This coincides well with the expectation of warm, moist low-level flow ahead of the surface cyclone (Fig. 1). Meanwhile, the significantly lower 850-hPa  $\theta_e$  anomalies in quadrant AnC highlight its unfavorable thermodynamic conditions for heavy precipitation. This also agrees with the expectation of CAA ahead of the surface anticyclone

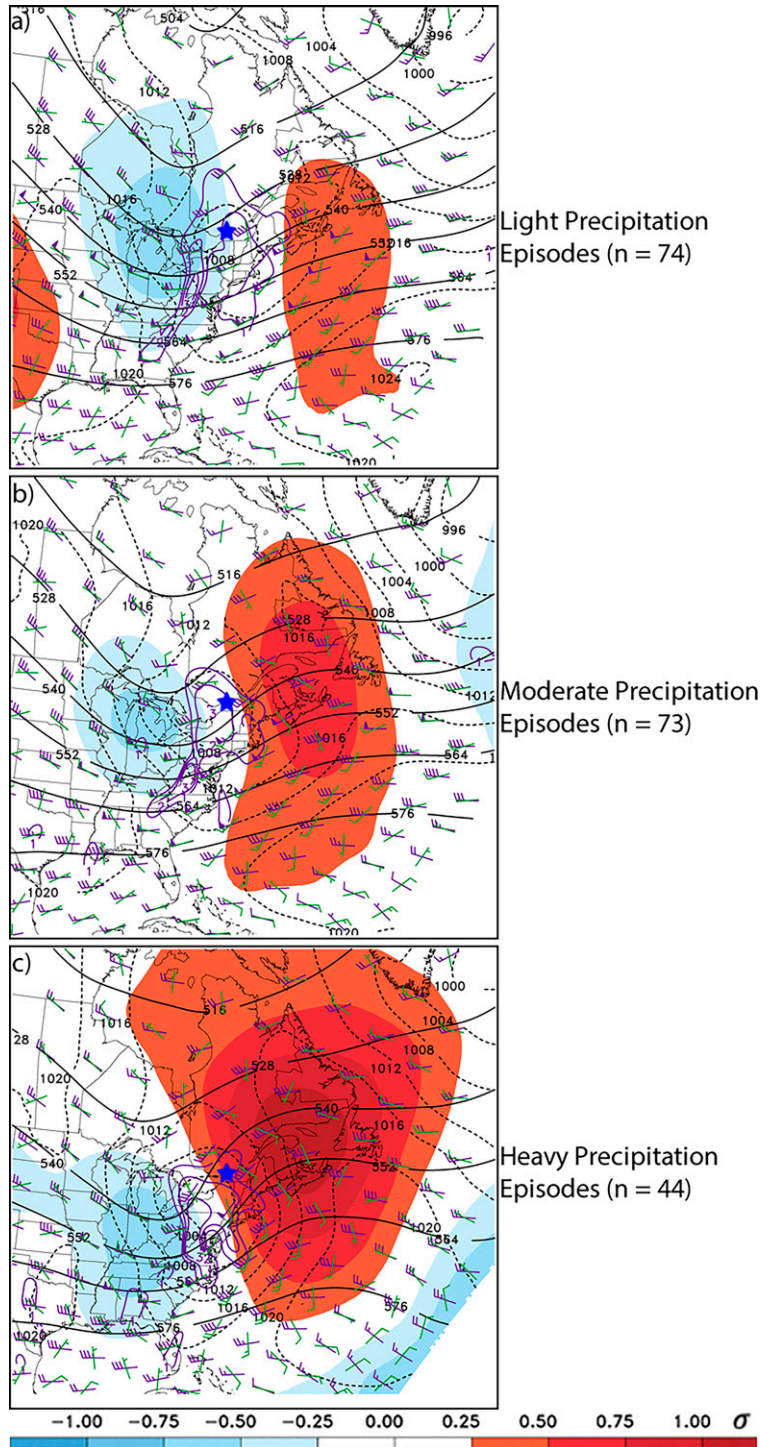


FIG. 9. Composites of 500-hPa geopotential height standardized anomalies ( $\sigma$ ; shaded), 500-hPa geopotential heights (dam; solid black contours), MSLP (hPa; dashed black contours), 500-hPa geostrophic absolute vorticity advection ( $\times 10^{-9} \text{ s}^{-2}$ ; solid purple contours for cyclonic vorticity advection only), 500-hPa winds (kt; purple bars;  $1 \text{ kt} \approx 0.51 \text{ m s}^{-1}$ ), and 1000-hPa winds (kt; green bars) for winter (a) light, (b) moderate, and (c) heavy CyC precipitation episodes at the onset time of the 6-h maximum precipitation. The blue star in each panel demarks the location of CYUL.

in quadrant AnC (Fig. 1). In general, the higher  $\theta_{em}$  (Fig. 6a) but lower  $\theta_{eT}$  (Fig. 6b) in quadrant CyC compared to quadrant AnW suggests that the thermodynamic conditions may be more favorable for heavy precipitation over a short period of time in quadrant CyC compared to quadrant AnW, but not over the entire quadrant period. We expand on this idea further using the synoptic composites in section 6.

#### d. Convective stability

Figures 7a and b show the Scheffé seasonal quadrant comparisons for  $\sigma_e$  [Eq. (2)] just prior to the maximum 6-h precipitation rate ( $\sigma_{em}$ ) and for the quadrant precipitation episode mean ( $\sigma_{eT}$ ), respectively. The  $\sigma_{em}$  and  $\sigma_{eT}$  are computed as in Eqs. (8) and (9), but with values of  $\sigma_e$ . Figures 7a,b show significantly lower  $\sigma_{eT}$  and  $\sigma_{em}$  in quadrant CyC compared to quadrants AnC and AnW in all seasons. The  $\sigma_{eT}$  and  $\sigma_{em}$  in quadrants CyW and CyC are generally not significantly different from one another except in winter when  $\sigma_{em}$  is significantly lower in quadrant CyC compared to quadrant CyW (Fig. 7a). From the interseasonal statistical comparisons (not shown), there are significantly lower (higher) values of  $\sigma_e$  in the summer (winter) in all quadrants.

One limitation to examining the distribution of convective (potential) instability in a climatology is that the choice of layer (e.g., 850–500 hPa) may not be ideal for every case. In other words, it may somewhat limit the ability to measure the variability of convectively unstable layers. Nevertheless, convective (potential) instability (i.e.,  $\sigma_e < 0$ ) within a given layer indicates that if that layer is lifted enough to reach saturation, it will become unstable with respect to moist air. While none of the 40-yr average  $\sigma_e$  values were negative, lower values may signal convective instability on the subgrid scale. In this case, even a modest amount of lift can destabilize the layer and facilitate enhanced ascent. Consequently, it corresponds well that the quadrants with the weakest convective stability (quadrants CyW and CyC) are also the quadrants with the largest values of ascent (Fig. 5) and the most intense precipitation (Fig. 4). Conversely, the most convectively stable quadrants (quadrants AnC and AnW) correspond to the quadrants with the lowest values of ascent (Fig. 5) and the least intense precipitation (Fig. 4).

The interseasonal  $\sigma_e$  results also provide insight on the summer precipitation results. Precipitation intensities in quadrants CyW and CyC are significantly different from one another in all seasons except summer, with weaker ascent in both quadrants compared to the other seasons. However, with very weak convective stability in quadrants CyW and CyC, subgrid scale ascent and precipitation from convective systems seems likely, suggesting that the synoptic-scale QG framework may be less useful in summer. We also observe a higher number of heavy precipitation episodes in quadrant AnC in the summer compared to any other season. The significantly smaller values of  $\sigma_e$  in the summer compared to the other seasons (Fig. 7) imply that less favorable synoptic-scale mechanisms for ascent in the summer can produce the same amount of precipitation at Montreal as in the other seasons, as also suggested by Milrad et al. (2014).

## 5. Odds ratios (ORs)

Figure 8 illustrates the ORs and associated 95% confidence intervals for light (Fig. 8a), moderate (Fig. 8b), and heavy (Fig. 8c) precipitation episodes. Figure 8a demonstrates significantly higher odds of light precipitation episodes occurring in quadrant CyC in all seasons with significantly lower odds in quadrant AnW. We observe significantly higher odds of moderate precipitation episodes in both quadrants CyW and CyC in all seasons and significantly lower odds in quadrants AnC and AnW (Fig. 8b). Quadrant CyW exhibits significantly higher odds for heavy precipitation episodes to occur in all seasons while quadrant CyC only has significantly higher odds in summer and fall. Quadrants AnC and AnW have significantly lower odds of heavy precipitation episodes in all seasons. Quadrants AnC and CyC also have significantly higher odds of very light precipitation episodes occurring in every season except fall for AnC and winter for CyC (not shown).

As Moore et al. (2019) used ORs to demonstrate the statistical association between Rossby wave breaking and extreme precipitation events, the ORs in Fig. 8c clearly indicate the strong statistical association between heavy precipitation episodes and quadrant CyW periods in Montreal. Moreover, the OR for heavy winter precipitation episodes of approximately one in quadrant CyC and 7.5 in quadrant CyW (meaning that the odds of a heavy precipitation episode are 7.5 times higher given that Montreal is in quadrant CyW compared to when Montreal is not) distinctly emphasizes the strong preference for heavy precipitation episodes to occur in quadrant CyW during the season (winter) when synoptic-scale mechanisms for ascent are most important. Figure 8 also demonstrates the consistent magnitude of the summer and fall ORs in quadrant CyC (~2) for all precipitation intensity categories. This suggests that precipitation has higher odds of occurring when Montreal is in quadrant CyC (in the summer and fall), but that the odds of a particular intensity occurring (i.e., light) are not much different than another (i.e., heavy).

## 6. Synoptic composites

Figure 9 displays winter composites of MSLP, 500-hPa geopotential heights, geopotential height standardized anomalies, and geostrophic cyclonic vorticity advection, as well as 500-hPa and 1000-hPa winds for the light, moderate, and heavy quadrant CyC precipitation episodes. Figure 10 is structured as in Fig. 9, but for 850-hPa geopotential heights, geostrophic temperature advection, winds,  $\theta_e$ , and  $\theta_e$  standardized anomalies. For an explanation of how the composite fields were calculated, please see section 2d. We produced and analyzed the same composite charts for the three other quadrants. However, for this paper we focus solely on quadrant CyC events in order to provide some physical insight into the preponderance of heavy precipitation episodes in this quadrant despite the implied cancellation between QG mechanisms for vertical motion. We leave an extended composite study as an avenue of future work.

The 500-hPa geopotential height standardized anomalies in Figs. 9a–c demonstrate a clear progression from a positively tilted 500-hPa trough–ridge couplet in the light composite to a

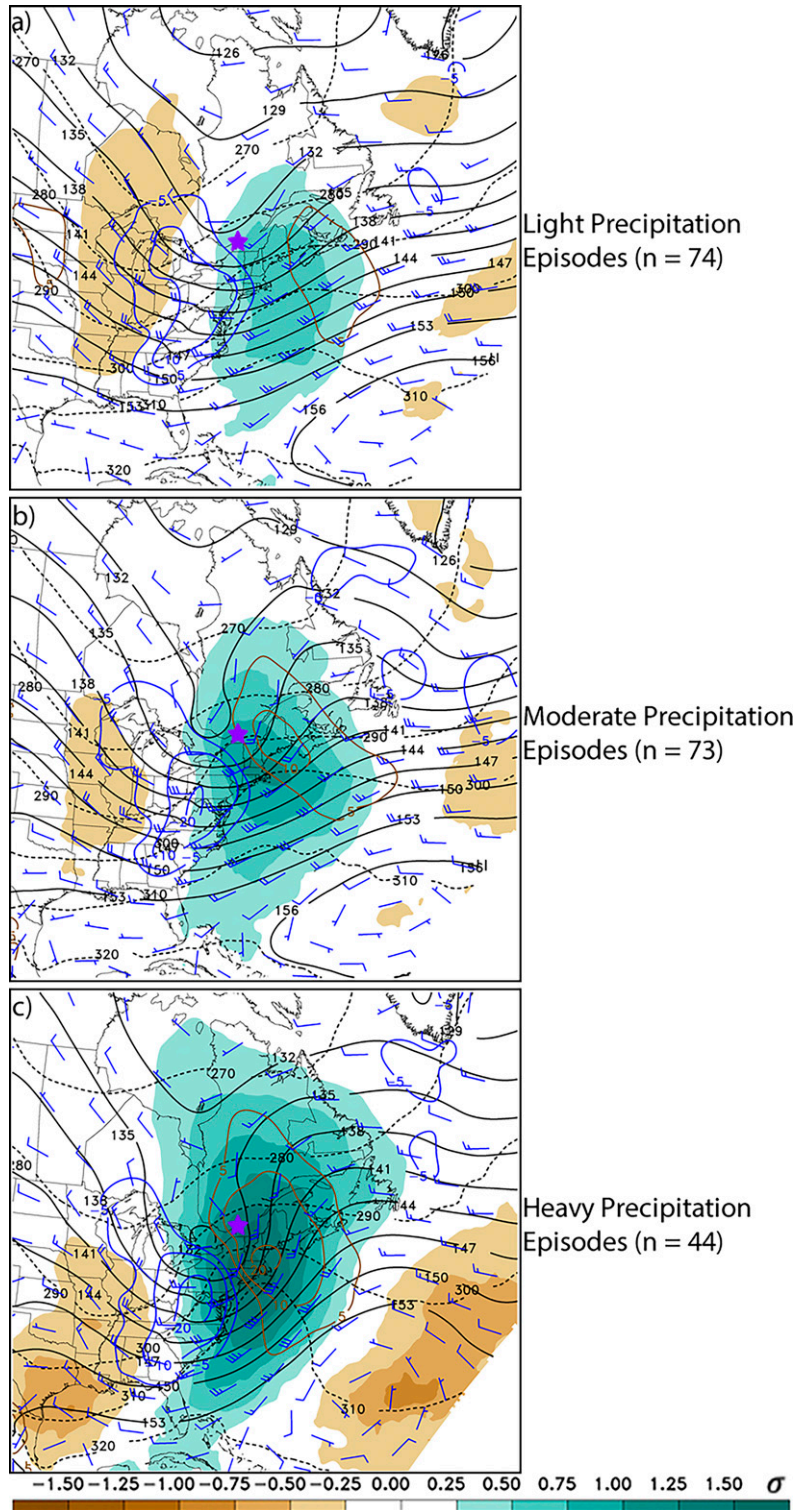


FIG. 10. As in Fig. 9, but for 850-hPa  $\theta_e$  standardized anomalies ( $\sigma$ ; shaded), 850-hPa  $\theta_e$  (K; dashed black contours), 850-hPa geopotential heights (dam; solid black contours), 850-hPa geostrophic temperature advection ( $\times 10^{-5} \text{ }^\circ\text{C s}^{-1}$ ; solid brown (blue) contours for warm (cold) air advection, and 850-hPa winds (kt; blue barbs). The purple star in each panel demarks the location of CYUL.

negatively tilted trough–ridge couplet in the heavy composite, as the orientation of the standardized anomaly gradient shifts from west-northwest–east-southeast in light episodes (Fig. 9a) to southwest–northeast in heavy episodes (Fig. 9c). The negatively tilted 500-hPa trough–ridge couplet represents a shortening of the wavelength between the trough and downstream ridge. From term B in Eq. (1), this implies stronger DCVA in moderate and heavy quadrant CyC precipitation episodes. This assertion is supported by the larger values of 500-hPa geostrophic CVA in moderate (Fig. 9b) and heavy (Fig. 9c) CyC episodes compared to light (Fig. 9a) episodes. In addition, while the composite surface cyclone strengthens only slightly from the light to the heavy category (Figs. 9a–c), the 1000-hPa winds near Montreal have more of an easterly component in the heavy composite, with a closed 1004-hPa contour located southeast of Montreal (Fig. 9c).

The composite structures in heavy quadrant CyC precipitation episodes (Fig. 9c) bear some resemblance to those depicted in Neiman and Shapiro (1993), of a surface cyclone located immediately upstream of an amplified and negatively tilted 500-hPa ridge, which is associated with a bent-back warm front (Shapiro and Keyser 1990). Shapiro and Keyser (1990), Neiman and Shapiro (1993), and Blier and Wakimoto (1995) demonstrated that both WAA and CAA can occur in association with a bent-back warm front. For this reason, Schultz et al. (1998) referred to these features more broadly as bent-back fronts. Figures 10b,c explicitly show that 850-hPa geostrophic WAA is present at Montreal in the moderate and particularly the heavy composite. Furthermore, the veering of the winds just east of Montreal from east-southeast at 1000 hPa (Fig. 9c) to south at 850 hPa (Fig. 10c) and southwest at 500 hPa (Fig. 9c) indicate 1000–500-hPa WAA in the heavy composite. However, just west of Montreal, the winds back from northwest at 1000 hPa to west at 850 hPa and southwest at 500 hPa, indicating 1000–500-hPa CAA. This suggests that in heavy CyC episodes, the most favorable QG mechanisms for ascent (DCVA combined with WAA) and heavy precipitation are ending at Montreal near the time of maximum precipitation, as CAA moves in from the west. Meanwhile, in the light composite, there is neutral 850-hPa temperature advection (Fig. 10a), while the winds show WAA between 1000 and 850 hPa and weak CAA between 850 and 500 hPa (Figs. 9a,10a).

Figures 10a–c also indicate progressively stronger positive  $\theta_e$  anomalies from the light to the heavy quadrant CyC precipitation episodes. This highlights more favorable thermodynamic conditions in the heavy episodes. However, the negative  $\theta_e$  advection just west of Montreal in all quadrant CyC precipitation episodes suggests that the favorable thermodynamic conditions for precipitation are also ending near the time of maximum precipitation.

The more amplified patterns observed in heavy winter quadrant CyC precipitation episodes (Figs. 9c, 10c) provide one likely explanation for the higher  $\theta_{em}$  in quadrant CyC compared to quadrant AnW in winter (Fig. 6a). This amplified pattern and negative tilt of the upstream 500-hPa trough results in strong DCVA, which facilitates a stronger surface cyclone downstream of the trough and a relatively short

period of continued warm, moist low-level flow from the Atlantic, leading to higher 850-hPa  $\theta_e$  anomalies near the time of maximum precipitation (Fig. 10c). However, as the 850-hPa trough passes and the 500-hPa trough approaches in CyC episodes, colder, drier air filters in with negative geostrophic advection of 850-hPa  $\theta_e$ , resulting in a decrease in the 850-hPa  $\theta_e$  anomalies near and west of Montreal (Figs. 10a–c).

The synoptic orientation is different in quadrant AnW (not shown), as there is a 500-hPa ridge located upstream of Montreal resulting in DAVA and a surface anticyclone downstream. Furthermore, AnW episodes follow AnC regimes, suggesting that the atmosphere is drier and colder prior to an AnW episode than a CyC episode, as the latter follows two quadrants (AnW and CyW) that feature WAA and moisture advection. Therefore, in a typical progression of a large-scale wave, there is more time for warm air and moisture to return to the region by the start of a CyC regime than an AnW regime.

## 7. Conclusions and future work

This study presents a conceptual synoptic model approach for a precipitation climatology. It differs from most previous precipitation climatologies because we use large-scale atmospheric structures to partition station precipitation data and identify precipitation episodes, as opposed to examining these structures in precipitation episodes identified using spatiotemporal or statistical criteria. We use the 500-hPa schematic shown in Fig. 1 as a simple metric to divide a 500-hPa wave into four quadrants based on the expected contributions toward vertical motion as implied by the QG- $\omega$  equation [Eq. (1)]. The precipitation observations are then grouped into their corresponding quadrants (Fig. 2).

For the 1979–2018 period, we identified 6230 quadrant precipitation episodes. Approximately 18% occurred in quadrant AnC, 12% in quadrant AnW, 34% in quadrant CyW, and 36% in quadrant CyC (Table 2). The proximity of the upstream 500-hPa trough provides one possible explanation for quadrant CyC having the highest percentage of precipitation episodes. The approach of the 500-hPa trough may trigger sufficient instability through steeper midlevel lapse rates and lift through DCVA to produce at least some precipitation. In particular, Fig. 7 demonstrates that convective stability values are lowest in quadrant CyC compared to the other quadrants in all seasons (except summer, when values are similar in quadrants CyW and CyC).

The most (least) intense precipitation occurs in quadrant CyW (AnC) in every season (Fig. 4). This agrees well with the expectations that WAA and DCVA contribute to unambiguous ascent in quadrant CyW and CAA and DAVA contribute to unambiguous descent in quadrant AnC. It follows that the average values of ascent are largest in quadrant CyW precipitation episodes and lowest in quadrant AnC precipitation episodes (Fig. 5b). Though these results could have been expected a priori, we would not have necessarily predicted quadrant CyC to have more intense precipitation than quadrant AnW.

As illustrated in Fig. 1, we expect both quadrants AnW and CyC to have competing QG mechanisms for vertical motion from TA and DVA. Nonetheless, Figs. 5a–b depict significantly larger values of 500-hPa ascent in quadrant CyC compared to quadrant AnW in all seasons. The negatively tilted 500-hPa trough in heavy quadrant CyC precipitation episodes (Fig. 9c) enhances and concentrates an area of DCVA over Montreal. Räisänen (1995) and Stepanyuk et al. (2017) also concluded that DCVA contributes more strongly to ascent than WAA in the midlatitudes. This suggests that TA and DVA may not be equally important to vertical motion forcing for a location like Montreal. A larger contribution to vertical motion from DVA compared to TA provides further insight into the stronger ascent and higher precipitation intensities in quadrant CyC compared to quadrant AnW. Furthermore, temperature advection in some quadrant CyC precipitation episodes may be relatively weak compared to DCVA (e.g., the light composite in Figs. 9a, 10a) or there may even be a period of WAA (e.g., the moderate and heavy composites in Figs. 10b,c). The presence of WAA for a period of time in the moderate and heavy CyC composites (Figs. 10b,c) is unexpected based on the simple conceptual model (Fig. 1) used to identify the quadrants, but aligns with the idea of a back-bent warm front (e.g., Shapiro and Keyser 1990; Neiman and Shapiro 1993) located near Montreal. One potential explanation for the unexpected WAA in the moderate and heavy composites is that the surface cyclone may not always be located precisely at the 500-hPa inflection point as the conceptual model dictates. As such, subtle details with respect to QG vertical motion-forcing mechanism sign, intensity, and timing are important in real-world analysis and forecast situations.

We observe significantly higher 850-hPa  $\theta_e$  standardized anomalies in quadrant CyW and significantly lower 850-hPa  $\theta_e$  standardized anomalies in quadrant AnC (Figs. 6a,b). Given the relationship between  $\theta_e$  and atmospheric stability and moisture content, this suggests that quadrant CyW (AnW) has the most (least) favorable thermodynamic conditions for precipitation. Quadrant CyC exhibits larger 850-hPa  $\theta_e$  standardized anomalies than quadrant AnW just prior to the maximum precipitation rate, with significantly larger anomalies in winter and fall (Fig. 6a). However, the mean 850-hPa  $\theta_e$  standardized anomalies over the entire quadrant precipitation episode were larger in quadrant AnW than CyC in all seasons except summer though they were not significantly different. In quadrant AnW, we observe slightly lower 850-hPa  $\theta_e$  anomalies in each of the intensity categories (not shown) compared to the respective composites of the same intensity category in quadrant CyC (Figs. 10a–c). However, we also observe positive 850-hPa  $\theta_e$  advection in each of the quadrant AnW composites while there is negative 850-hPa  $\theta_e$  advection in each of the quadrant CyC composites, just west of Montreal. This suggests that while there may be a relatively short period of elevated  $\theta_e$  anomalies in quadrant CyC close to the time of maximum precipitation (especially in heavy quadrant CyC precipitation episodes; Fig. 10c), the elevated  $\theta_e$  anomalies are quickly eroded as colder, drier air filters in

with the passage of the 850-hPa trough and the approach of the 500-hPa trough.

Using ORs (Fig. 8), we can deduce the preponderance of precipitation episodes of different intensity (Table 1) in the four quadrants. We find significantly higher odds of heavy precipitation episodes in every season in quadrant CyW with the highest odds in winter and spring. Quadrants AnC and AnW have significantly lower odds of heavy precipitation episodes in all seasons. In quadrant CyC, we find significantly higher odds of heavy precipitation episodes in summer and fall (with lower ORs than in quadrant CyW) and significantly higher odds of light and moderate precipitation episodes in every season. Therefore, operational meteorologists should pay particular attention to the possibility of heavy precipitation when Montreal is in quadrant CyW, especially in the winter and spring. One of the defining features of heavy quadrant CyC precipitation episodes in the fall (not shown) and winter (Fig. 9) is a negatively tilted trough–ridge couplet at 500 hPa. Given the higher predictability of 500-hPa geopotential heights in NWP models compared to QPF (Roebber and Bosart 1998; Sisson and Gyakum 2004), this feature of heavy quadrant CyC precipitation episodes may be of particular interest to operational meteorologists.

We obtained similar results to those in Figs. 4–7 for Burlington, Vermont (not shown), including the heavier precipitation observed in quadrant CyC compared to quadrant AnW. Although the most intense precipitation generally occurs when the synoptic pattern favors unambiguous QG ascent (quadrant CyW), precipitation (especially heavy episodes) is more likely to occur in quadrant CyC than quadrant AnW despite both quadrants having competing QG mechanisms for ascent. Additional precipitation climatologies that apply the quadrant method to other midlatitude locations may provide further insight into whether this particular result is regionally, or topographically dependent.

Future work should also include a more in-depth composite analysis of the large-scale meteorological patterns (LSMPs; e.g., Barlow et al. 2019) associated with light, moderate, and heavy precipitation episodes. This might incorporate analyses of Q-vectors, frontogenesis, moisture flux, and thermodynamic diagrams before and during precipitation episodes, as previously done in numerous composite studies (Milrad et al. 2010, 2014; Dookhie 2011; Ressler et al. 2012). Finally, individual precipitation events tend not to be well represented in subseasonal and seasonal forecasts (e.g., Pan et al. 2019; Dickinson et al. 2021) as well as climate simulations (e.g., Dominguez et al. 2012). Consequently, the quadrant approach (using 500-hPa geopotential heights) presented in this paper could provide a useful metric to assess the likelihood of occurrence of heavy precipitation episodes in subseasonal and seasonal predictions as well as the LSMPs associated with heavy precipitation episodes in a changing climate.

*Acknowledgments.* Thanks to the NOAA National Centers for Environmental Information (NCEI) for providing access to the 6-h precipitation data, and the NOAA Earth System Research Laboratory (ESRL) Physical Sciences

Division (PSD) for providing access to the NARR. This study was funded in part by a Natural Sciences and Engineering Research Council (NSERC) Canada Graduate Scholarship—Master's Program (CGS M), as well as an NSERC Discovery Grant RGPIN-2016-04916 and a Fonds de recherche du Québec—Nature et Technologies (FRQNT) Team Grant 253572.

*Data availability statement.* The 6-h Montreal precipitation data and code used in this study are available from the authors upon request. The 1979–2008 precipitation data were retrieved from the authors of Milrad et al. (2014). The 2009–18 data were obtained using archived synoptic (SYNOP) reports from <https://www.ogimet.com/synops.phtml.en>. The NARR data were downloaded from NOAA/OAR/ESRL PSD, Boulder, Colorado, and are available online at <https://psl.noaa.gov/data/gridded/data.narr.html>. To help make this study more reproducible, our complete list of precipitation episodes including amounts and duration, and partitioned by quadrant, is freely available for download at <https://wx.erau.edu/faculty/milrads/YULprecipdates.xlsx>.

#### REFERENCES

- Akinremi, O. O., S. M. McGinn, and H. W. Cutforth, 1999: Precipitation trends on the Canadian prairies. *J. Climate*, **12**, 2996–3003, [https://doi.org/10.1175/1520-0442\(1999\)012<2996:PTOTCP>2.0.CO;2](https://doi.org/10.1175/1520-0442(1999)012<2996:PTOTCP>2.0.CO;2).
- Barlow, M., and Coauthors, 2019: North American extreme precipitation events and related large-scale meteorological patterns: A review of statistical methods, dynamics, modeling, and trends. *Climate Dyn.*, **53**, 6835–6875, <https://doi.org/10.1007/s00382-019-04958-z>.
- Barton, Y., P. Giannakaki, H. von Waldow, C. Chevalier, S. Pfahl, and O. Martius, 2016: Clustering of regional-scale extreme precipitation events in southern Switzerland. *Mon. Wea. Rev.*, **144**, 347–369, <https://doi.org/10.1175/MWR-D-15-0205.1>.
- Billingsley, D., 1997: Review of QG theory—Part II: The omega equation. *Natl. Wea. Dig.*, **21**, 43–51.
- Blier, W., and R. M. Wakimoto, 1995: Observations of the early evolution of an explosive oceanic cyclone during ERICA IOP 5. Part I: Synoptic overview and mesoscale frontal structure. *Mon. Wea. Rev.*, **123**, 1288–1310, [https://doi.org/10.1175/1520-0493\(1995\)123<1288:OOTEEO>2.0.CO;2](https://doi.org/10.1175/1520-0493(1995)123<1288:OOTEEO>2.0.CO;2).
- Bluestein, H. B., 1992: *Principles of Kinematics and Dynamics*. Vol. 1, *Synoptic-Dynamic Meteorology in Midlatitudes*, Oxford University Press, 431 pp.
- Dickinson, T. A., M. B. Richman, and J. C. Furtado, 2021: Sub-seasonal-to-seasonal extreme precipitation events in the contiguous United States: Generation of a database and climatology. *J. Climate*, **34**, 7571–7586, <https://doi.org/10.1175/JCLI-D-20-0580.1>.
- Dominguez, F., E. Rivera, D. Lettenmaier, and C. Castro, 2012: Changes in winter precipitation extremes for the western United States under a warmer climate as simulated by regional climate models. *Geophys. Res. Lett.*, **39**, L05803, <https://doi.org/10.1029/2011GL050762>.
- Dookhie, G. C., 2011: Dynamics of heavy warm-season precipitation events in Montreal. M.S. thesis, Dept. of Atmospheric and Oceanic Sciences, McGill University, 95 pp.
- Durrán, D. R., and L. W. Snellman, 1987: The diagnosis of synoptic-scale vertical motion in an operational environment. *Wea. Forecasting*, **2**, 17–31, [https://doi.org/10.1175/1520-0434\(1987\)002<0017:TDOSSV>2.0.CO;2](https://doi.org/10.1175/1520-0434(1987)002<0017:TDOSSV>2.0.CO;2).
- Fischer, A. P., 1998: A synoptic climatology of Montreal precipitation. M.S. thesis, Dept. of Atmospheric and Oceanic Sciences, McGill University, 79 pp.
- Fukutome, S., M. A. Liniger, and M. Süveges, 2015: Automatic threshold and run parameter selection: A climatology for extreme hourly precipitation in Switzerland. *Theor. Appl. Climatol.*, **120**, 403–416, <https://doi.org/10.1007/s00704-014-1180-5>.
- Funk, T., 2011: A practical, basic guide to quasi-geostrophic theory, response to geostrophic deformation, ageostrophic motion and jet streaks. National Weather Service, Louisville, KY, 26 pp., [https://www.weather.gov/media/lmk/soo/QG\\_Theory\\_Review.pdf](https://www.weather.gov/media/lmk/soo/QG_Theory_Review.pdf).
- Grumm, R. H., and R. Hart, 2001: Standardized anomalies applied to significant cold season weather events: Preliminary findings. *Wea. Forecasting*, **16**, 736–754, [https://doi.org/10.1175/1520-0434\(2001\)016<0736:SAATSC>2.0.CO;2](https://doi.org/10.1175/1520-0434(2001)016<0736:SAATSC>2.0.CO;2).
- Hoskins, B., I. Draghici, and H. C. Davies, 1978: A new look at the  $\omega$ -equation. *Quart. J. Roy. Meteor. Soc.*, **104**, 31–38, <https://doi.org/10.1002/qj.49710443903>.
- Konrad, C. E., II, 1997: Synoptic-scale features associated with warm season heavy rainfall over the interior southeastern United States. *Wea. Forecasting*, **12**, 557–571, [https://doi.org/10.1175/1520-0434\(1997\)012<0557:SSFAWW>2.0.CO;2](https://doi.org/10.1175/1520-0434(1997)012<0557:SSFAWW>2.0.CO;2).
- Kunkel, K. E., K. Andsager, and D. R. Easterling, 1999: Long-term trends in extreme precipitation events over the conterminous United States and Canada. *J. Climate*, **12**, 2515–2527, [https://doi.org/10.1175/1520-0442\(1999\)012<2515:LTTEP>2.0.CO;2](https://doi.org/10.1175/1520-0442(1999)012<2515:LTTEP>2.0.CO;2).
- Kutner, M. H., C. J. Nachtsheim, J. Neter, and W. Li, 2005: *Applied Linear Statistical Models*. Vol. 5, McGraw-Hill, 1415 pp.
- Mesinger, F., and Coauthors, 2006: North American Regional Reanalysis. *Bull. Amer. Meteor. Soc.*, **87**, 343–360, <https://doi.org/10.1175/BAMS-87-3-343>.
- Milrad, S. M., E. H. Atallah, and J. R. Gyakum, 2009: Synoptic-scale characteristics and precursors of cool-season precipitation events at St. John's Newfoundland, 1979–2005. *Wea. Forecasting*, **24**, 667–689, <https://doi.org/10.1175/2008WAF2222167.1>.
- , —, and —, 2010: Synoptic typing of extreme cool-season precipitation events at St. John's, Newfoundland, 1979–2005. *Wea. Forecasting*, **25**, 562–586, <https://doi.org/10.1175/2009WAF2222301.1>.
- , —, J. H. Gyakum, and G. Dookhie, 2014: Synoptic typing and precursors of heavy warm-season precipitation events at Montreal, Québec. *Wea. Forecasting*, **29**, 419–444, <https://doi.org/10.1175/WAF-D-13-00030.1>.
- Moore, B. J., K. M. Mahoney, E. M. Sukovich, R. Cifelli, and T. M. Hamill, 2015: Climatology and environmental characteristics of extreme precipitation events in the southeastern United States. *Mon. Wea. Rev.*, **143**, 718–741, <https://doi.org/10.1175/MWR-D-14-00065.1>.
- , D. Keyser, and L. F. Bosart, 2019: Linkages between extreme precipitation events in the central and eastern United States and Rossby wave breaking. *Mon. Wea. Rev.*, **147**, 3327–3349, <https://doi.org/10.1175/MWR-D-19-0047.1>.
- Neiman, P. J., and M. Shapiro, 1993: The life cycle of an extratropical marine cyclone. Part I: Frontal-cyclone evolution and thermodynamic air–sea interaction. *Mon. Wea. Rev.*, **121**,

- 2153–2176, [https://doi.org/10.1175/1520-0493\(1993\)121<2153:TLCOAE>2.0.CO;2](https://doi.org/10.1175/1520-0493(1993)121<2153:TLCOAE>2.0.CO;2).
- Pan, B., K. Hsu, A. AghaKouchak, S. Sorooshian, and W. Higgins, 2019: Precipitation prediction skill for the West Coast United States: From short to extended range. *J. Climate*, **32**, 161–182, <https://doi.org/10.1175/JCLI-D-18-0355.1>.
- Räisänen, J., 1995: Factors affecting synoptic-scale vertical motions: A statistical study using a generalized omega equation. *Mon. Wea. Rev.*, **123**, 2447–2460, [https://doi.org/10.1175/1520-0493\(1995\)123<2447:FASSVM>2.0.CO;2](https://doi.org/10.1175/1520-0493(1995)123<2447:FASSVM>2.0.CO;2).
- Regan, M., 1998: Canadian ice storm 1998. *WMO Bull.*, **47**, 250–256.
- Ressler, G. M., S. M. Milrad, E. H. Atallah, and J. R. Gyakum, 2012: Synoptic-scale analysis of freezing rain events in Montreal, Quebec, Canada. *Wea. Forecasting*, **27**, 362–378, <https://doi.org/10.1175/WAF-D-11-00071.1>.
- Rochette, S. M., P. S. Market, C. M. Gravelle, and T. A. Niziol, 2017: A case study of anomalous snowfall with an Alberta Clipper. *Adv. Meteor.*, **2017**, 8406379, <https://doi.org/10.1155/2017/8406379>.
- Roebber, P. J., and L. F. Bosart, 1998: The sensitivity of precipitation to circulation details. Part I: An analysis of regional analogs. *Mon. Wea. Rev.*, **126**, 437–455, [https://doi.org/10.1175/1520-0493\(1998\)126<0437:TSOPTC>2.0.CO;2](https://doi.org/10.1175/1520-0493(1998)126<0437:TSOPTC>2.0.CO;2).
- Schultz, D. M., D. Keyser, and L. F. Bosart, 1998: The effect of large-scale flow on low-level frontal structure and evolution in midlatitude cyclones. *Mon. Wea. Rev.*, **126**, 1767–1791, [https://doi.org/10.1175/1520-0493\(1998\)126<1767:TEOLSF>2.0.CO;2](https://doi.org/10.1175/1520-0493(1998)126<1767:TEOLSF>2.0.CO;2).
- Shapiro, M., and D. Keyser, 1990: Fronts, jet streams, and the tropopause. *Extratropical Cyclones: The Erik Palmén Memorial Volume*, C. Newton and E. O. Holopainen, Eds., Amer. Meteor. Soc., 167–191.
- Sisson, P. A., and J. R. Gyakum, 2004: Synoptic-scale precursors to significant cold-season precipitation events in Burlington, Vermont. *Wea. Forecasting*, **19**, 841–854, [https://doi.org/10.1175/1520-0434\(2004\)019<0841:SPTSCP>2.0.CO;2](https://doi.org/10.1175/1520-0434(2004)019<0841:SPTSCP>2.0.CO;2).
- Soulard, F., 1998: The St. Lawrence River Valley 1998 Ice Storm: Maps and facts. *Geomatica*, **52**, 310–324.
- Stepanyuk, O., J. Räisänen, V. A. Sinclair, and H. Järvinen, 2017: Factors affecting atmospheric vertical motions as analyzed with a generalized omega equation and the OpenIFS model. *Tellus*, **69A**, 1271563, <https://doi.org/10.1080/16000870.2016.1271563>.
- Trenberth, K. E., 1978: On the interpretation of the diagnostic quasi-geostrophic omega equation. *Mon. Wea. Rev.*, **106**, 131–137, [https://doi.org/10.1175/1520-0493\(1978\)106<0131:OTIOTD>2.0.CO;2](https://doi.org/10.1175/1520-0493(1978)106<0131:OTIOTD>2.0.CO;2).
- Wang, Y., and L. Zhou, 2005: Observed trends in extreme precipitation events in China during 1961–2001 and the associated changes in large-scale circulation. *Geophys. Res. Lett.*, **32**, L09707, <https://doi.org/10.1029/2005GL023769>.
- Wilks, D. S., 2006: *Statistical Methods in the Atmospheric Sciences*. 2nd ed. International Geophysics Series, Vol. 100, Academic Press, 648 pp.
- Yu, R., Y. Xu, T. Zhou, and J. Li, 2007: Relation between rainfall duration and diurnal variation in the warm season precipitation over central eastern China. *Geophys. Res. Lett.*, **34**, L13703, <https://doi.org/10.1029/2007GL030315>.

Copyright of Weather & Forecasting is the property of American Meteorological Society and its content may not be copied or emailed to multiple sites or posted to a listserv without the copyright holder's express written permission. However, users may print, download, or email articles for individual use.